Wide-field high-speed space-division multiplexing optical coherence tomography using an integrated photonic device

YONGYANG HUANG,[1,2] MUDABBIR BADAR,[1,2] ARTHUR NITKOWSKI,[3] AARON WEINROTH,[3] NELSON TANSU,[1,2] AND CHAO ZHOU[1,2,4,*]

[1]*Department of Electrical and Computer Engineering, Lehigh University, 27 Memorial Drive W, Bethlehem, PA 18015, USA*

[2]*Center for Photonics and Nanoelectronics, Lehigh University, 27 Memorial Drive W, Bethlehem, PA 18015, USA*

[3]*Tornado Spectral Systems, Inc., 555 Richmond Street West, Suite 402, Toronto, ON, M5V 3B1, Canada*

[4] *Department of Bioengineering, Lehigh University, Bethlehem, PA 18015*

chaozhou@lehigh.edu

Abstract: Space-division multiplexing optical coherence tomography (SDM-OCT) is a recently developed parallel OCT imaging method in order to achieve multi-fold speed improvement. However, the assembly of fiber optics components used in the first prototype system was labor-intensive and susceptible to errors. Here, we demonstrate a high-speed SDM-OCT system using an integrated photonic chip that can be reliably manufactured with high precisions and low per-unit cost. A three-layer cascade of 1×2 splitters was integrated in the photonic chip to split the incident light into 8 parallel imaging channels with ~3.7 mm optical delay in air between each channel. High-speed imaging (~1s/volume) of porcine eyes ex vivo and wide-field imaging (~18.0 × 14.3 mm^2) of human fingers in vivo were demonstrated with the chip-based SDM-OCT system.

OCIS codes: (060.4230) Multiplexing; (110.4500) Optical Coherence Tomography; (110.6880) Three-dimensional Image Acquisition; (130.0130) Integrated Optics; (170.0110) Imaging Systems; (170.3880) Medical and Biological Imaging.

References and links

1. D. Huang, E. A. Swanson, C. P. Lin, J. S. Schuman, W. G. Stinson, W. Chang, M. R. Hee, T. Flotte, K. Gregory, C. A. Puliafito, and J. G. Fujimoto, "Optical Coherence Tomography," Science **254**, 1178-1181 (1991).
2. M. Wojtkowski, "High-speed optical coherence tomography: basics and applications," Applied Optics **49**, D30-61 (2010).
3. W. Drexler, M. Liu, A. Kumar, T. Kamali, A. Unterhuber, and R. A. Leitgeb, "Optical coherence tomography today: speed, contrast, and multimodality," Journal of Biomedical Optics **19**, 071412 (2014).
4. J. Fujimoto and E. Swanson, "The Development, Commercialization, and Impact of Optical Coherence TomographyHistory of Optical Coherence Tomography," Investigative Ophthalmology & Visual Science **57**, OCT1-OCT13 (2016).
5. T. Klein and R. Huber, "High-speed OCT light sources and systems [Invited]," Biomedical Optics Express **8**, 828-859 (2017).
6. M. Choma, M. Sarunic, C. Yang, and J. Izatt, "Sensitivity advantage of swept source and Fourier domain optical coherence tomography," Optics Express **11**, 2183-2189 (2003).
7. R. Leitgeb, C. Hitzenberger, and A. Fercher, "Performance of fourier domain vs. time domain optical coherence tomography," Optics Express **11**, 889-894 (2003).
8. W. Wieser, B. R. Biedermann, T. Klein, C. M. Eigenwillig, and R. Huber, "Multi-Megahertz OCT: High quality 3D imaging at 20 million A-scans and 4.5 GVoxels per second," Optics Express **18**, 14685-14704 (2010).
9. I. Grulkowski, J. J. Liu, B. Potsaid, V. Jayaraman, C. D. Lu, J. Jiang, A. E. Cable, J. S. Duker, and J. G. Fujimoto, "Retinal, anterior segment and full eye imaging using ultrahigh speed swept source OCT with vertical-cavity surface emitting lasers," Biomedical Optics Express **3**, 2733-2751 (2012).

10. B. Povazay, B. Hofer, C. Torti, B. Hermann, A. R. Tumlinson, M. Esmaeelpour, C. A. Egan, A. C. Bird, and W. Drexler, "Impact of enhanced resolution, speed and penetration on three-dimensional retinal optical coherence tomography," Optics Express **17**, 4134 (2009).
11. T. Klein, W. Wieser, C. M. Eigenwillig, B. R. Biedermann, and R. Huber, "Megahertz OCT for ultrawide-field retinal imaging with a 1050nm Fourier domain mode-locked laser," Optics Express **19**, 3044-3062 (2011).
12. T. Klein, W. Wieser, L. Reznicek, A. Neubauer, A. Kampik, and R. Huber, "Multi-MHz retinal OCT," Biomedical Optics Express **4**, 1890-1908 (2013).
13. C. D. Lu, M. F. Kraus, B. Potsaid, J. J. Liu, W. Choi, V. Jayaraman, A. E. Cable, J. Hornegger, J. S. Duker, and J. G. Fujimoto, "Handheld ultrahigh speed swept source optical coherence tomography instrument using a MEMS scanning mirror," Biomedical Optics Express **5**, 293-311 (2013).
14. L. Reznicek, T. Klein, W. Wieser, M. Kernt, A. Wolf, C. Haritoglou, A. Kampik, R. Huber, and A. S. Neubauer, "Megahertz ultra-wide-field swept-source retina optical coherence tomography compared to current existing imaging devices," Graefe's Archive for Clinical and Experimental Ophthalmology **252**, 1009-1016 (2014).
15. J. P. Kolb, T. Klein, C. L. Kufner, W. Wieser, A. S. Neubauer, and R. Huber, "Ultra-widefield retinal MHz-OCT imaging with up to 100 degrees viewing angle," Biomed. Opt. Express **6**, 1534-1552 (2015).
16. K. J. Mohler, W. Draxinger, T. Klein, J. P. Kolb, W. Wieser, C. Haritoglou, A. Kampik, J. G. Fujimoto, A. S. Neubauer, R. Huber, and A. Wolf, "Combined 60° Wide-Field Choroidal Thickness Maps and High-Definition En Face Vasculature Visualization Using Swept-Source Megahertz OCT at 1050 nm," Investigative Ophthalmology & Visual Science **56**, 6284 (2015).
17. T.-H. Tsai, B. Potsaid, Y. K. Tao, V. Jayaraman, J. Jiang, P. J. S. Heim, M. F. Kraus, C. Zhou, J. Hornegger, H. Mashimo, A. E. Cable, and J. G. Fujimoto, "Ultrahigh speed endoscopic optical coherence tomography using micromotor imaging catheter and VCSEL technology," Biomedical Optics Express **4**, 1119 (2013).
18. T. Wang, T. Pfeiffer, E. Regar, W. Wieser, H. van Beusekom, C. T. Lancee, G. Springeling, I. Krabbendam, A. F. W. van der Steen, R. Huber, and G. van Soest, "Heartbeat OCT: in vivo intravascular megahertz-optical coherence tomography," Biomedical Optics Express **6**, 5021-5032 (2015).
19. B. Baumann, B. Potsaid, M. F. Kraus, J. J. Liu, D. Huang, J. Hornegger, A. E. Cable, J. S. Duker, and J. G. Fujimoto, "Total retinal blood flow measurement with ultrahigh speed swept source/Fourier domain OCT," Biomedical Optics Express **2**, 1539-1552 (2011).
20. M. F. Kraus, B. Potsaid, M. A. Mayer, R. Bock, B. Baumann, J. J. Liu, J. Hornegger, and J. G. Fujimoto, "Motion correction in optical coherence tomography volumes on a per A-scan basis using orthogonal scan patterns," Biomedical Optics Express **3**, 1182-1199 (2012).
21. Q. Zhang, Y. Huang, T. Zhang, S. Kubach, L. An, M. Laron, U. Sharma, and R. K. Wang, "Wide-field imaging of retinal vasculature using optical coherence tomography-based microangiography provided by motion tracking," Journal of Biomedical Optics **20**, 066008-066008 (2015).
22. W. Wei, J. Xu, U. Baran, S. Song, W. Qin, X. Qi, and R. K. Wang, "Intervolume analysis to achieve four-dimensional optical microangiography for observation of dynamic blood flow," Journal of Biomedical Optics **21**, 036005-036005 (2016).
23. U. Baran, W. Wei, J. Xu, X. Qi, W. O. Davis, and R. K. Wang, "Video-rate volumetric optical coherence tomography-based microangiography," Optical Engineering **55**, 040503-040503 (2016).
24. A. Kowalczyk, B. J. Kaluzny, K. Karnowski, M. Szkulmowski, M. Wojtkowski, M. Gora, and R. Huber, "Ultra high-speed swept source OCT imaging of the anterior segment of human eye at 200 kHz with adjustable imaging range," Optics Express **17**, 14880-14894 (2009).
25. J. Xu, W. Wei, S. Song, X. Qi, and R. K. Wang, "Scalable wide-field optical coherence tomography-based angiography for in vivo imaging applications," Biomedical Optics Express **7**, 1905-1919 (2016).
26. W. Chen, J. You, X. Gu, C. Du, and Y. Pan, "High-speed swept source optical coherence Doppler tomography for deep brain microvascular imaging," Scientific Reports **6**, 38786 (2016).
27. O. Assayag, M. Antoine, B. Sigal-Zafrani, M. Riben, F. Harms, A. Burcheri, K. Grieve, E. Dalimier, B. Le Conte de Poly, and C. Boccara, "Large Field, High Resolution Full-Field Optical Coherence Tomography: A Pre-Clinical Study of Human Breast Tissue and Cancer Assessment," Technol Cancer Res Treat **13**, 455-468 (2014).
28. S. Song, J. Xu, and R. K. Wang, "Long-range and wide field of view optical coherence tomography for in vivo 3D imaging of large volume object based on akinetic programmable swept source," Biomedical Optics Express **7**, 4734-4748 (2016).
29. E. Min, J. Lee, A. Vavilin, S. Jung, S. Shin, J. Kim, and W. Jung, "Wide-field optical coherence microscopy of the mouse brain slice," Optics Letters **40**, 4420-4423 (2015).
30. H. C. Hendargo, R. Estrada, S. J. Chiu, C. Tomasi, S. Farsiu, and J. A. Izatt, "Automated non-rigid registration and mosaicing for robust imaging of distinct retinal capillary beds using speckle variance optical coherence tomography," Biomedical Optics Express **4**, 803-821 (2013).
31. R. J. Zawadzki, S. S. Choi, A. R. Fuller, J. W. Evans, B. Hamann, and J. S. Werner, "Cellular resolution volumetric in vivo retinal imaging with adaptive optics–optical coherence tomography," Optics Express **17**, 4084 (2009).
32. S. H. Yun, C. Boudoux, G. J. Tearney, and B. E. Bouma, "High-speed wavelength-swept semiconductor laser with a polygon-scanner-based wavelength filter," Opt. Lett. **28**, 1981 (2003).

33. M. A. Choma, K. Hsu, and J. A. Izatt, "Swept source optical coherence tomography using an all-fiber 1300 nm ring laser source," J. Biomed. Opt **10**, 044009-044009-044006 (2005).
34. C. Jun, M. Villiger, W.-Y. Oh, and B. E. Bouma, "All-fiber wavelength swept ring laser based on Fabry-Perot filter for optical frequency domain imaging," Opt. Express **22**, 25805-25814 (2014).
35. M. Bonesi, M. P. Minneman, J. Ensher, B. Zabihian, H. Sattmann, P. Boschert, E. Hoover, R. A. Leitgeb, M. Crawford, and W. Drexler, "Akinetic all-semiconductor programmable swept-source at 1550 nm and 1310 nm with centimeters coherence length," Opt. Express **22**, 2632 (2014).
36. B. Potsaid, B. Baumann, D. Huang, S. Barry, A. E. Cable, J. S. Schuman, J. S. Duker, and J. G. Fujimoto, "Ultrahigh speed 1050nm swept source/Fourier domain OCT retinal and anterior segment imaging at 100,000 to 400,000 axial scans per second," Optics Express **18**, 20029-20048 (2010).
37. S. Zotter, M. Pircher, T. Torzicky, M. Bonesi, E. Götzinger, R. A. Leitgeb, and C. K. Hitzenberger, "Visualization of microvasculature by dual-beam phase-resolved Doppler optical coherence tomography," Optics Express **19**, 1217-1227 (2011).
38. C. Blatter, S. Coquoz, B. Grajciar, A. S. G. Singh, M. Bonesi, R. M. Werkmeister, L. Schmetterer, and R. A. Leitgeb, "Dove prism based rotating dual beam bidirectional Doppler OCT," Biomedical Optics Express **4**, 1188-1203 (2013).
39. W. Trasischker, R. M. Werkmeister, S. Zotter, B. Baumann, T. Torzicky, M. Pircher, and C. K. Hitzenberger, "In vitroand in vivothree-dimensional velocity vector measurement by three-beam spectral-domain Doppler optical coherence tomography," Journal of Biomedical Optics **18**, 116010 (2013).
40. H. Y. Lee, H. Sudkamp, T. Marvdashti, and A. K. Ellerbee, "Interleaved optical coherence tomography," Optics Express **21**, 26542-26556 (2013).
41. H. Y. Lee, T. Marvdashti, L. Duan, S. A. Khan, and A. K. Ellerbee, "Scalable multiplexing for parallel imaging with interleaved optical coherence tomography," Biomedical Optics Express **5**, 3192 (2014).
42. L. Duan, H. Y. Lee, G. Lee, M. Agrawal, G. T. Smith, and A. K. Ellerbee, "Single-shot speckle noise reduction by interleaved optical coherence tomography," Journal of Biomedical Optics **19**, 120501-120501 (2014).
43. L. Duan, T. Marvdashti, and A. K. Ellerbee, "Polarization-sensitive interleaved optical coherence tomography," Optics Express **23**, 13693-13703 (2015).
44. C. Zhou, A. Alex, J. Rasakanthan, and Y. Ma, "Space-division multiplexing optical coherence tomography," Optics Express **21**, 19219-19227 (2013).
45. G. Yurtsever, B. Považay, A. Alex, B. Zabihian, W. Drexler, and R. Baets, "Photonic integrated Mach-Zehnder interferometer with an on-chip reference arm for optical coherence tomography," Biomedical Optics Express **5**, 1050-1061 (2014).
46. G. Yurtsever, N. Weiss, J. Kalkman, T. G. van Leeuwen, and R. Baets, "Ultra-compact silicon photonic integrated interferometer for swept-source optical coherence tomography," Optics Letters **39**, 5228-5231 (2014).
47. L. Chang, N. Weiss, T. G. van Leeuwen, M. Pollnau, R. M. de Ridder, K. Wörhoff, V. Subramaniam, and J. S. Kanger, "Chip based common-path optical coherence tomography system with an on-chip microlens and multi-reference suppression algorithm," Optics Express **24**, 12635-12650 (2016).
48. K. Preston, A. Nitkowski, N. Sherwood-Droz, B. S. Schmidt, and A. R. Hajian, "On-chip spectrometer for low-cost optical coherence tomography," Technical Proceedings of the 2014 NSTI Nanotechnology Conference and Expo, NSTI-Nanotech 2014 **2**, 435-438 (2014).
49. O. O. Ahsen, Y. K. Tao, B. M. Potsaid, Y. Sheikine, J. Jiang, I. Grulkowski, T.-H. Tsai, V. Jayaraman, M. F. Kraus, J. L. Connolly, J. Hornegger, A. Cable, and J. G. Fujimoto, "Swept source optical coherence microscopy using a 1310 nm VCSEL light source," Optics Express **21**, 18021 (2013).
50. Z. Wang, B. Potsaid, L. Chen, C. Doerr, H.-C. Lee, T. Nielson, V. Jayaraman, A. E. Cable, E. Swanson, and J. G. Fujimoto, "Cubic meter volume optical coherence tomography," Optica **3**, 1496-1503 (2016).
51. T. Pfeiffer, W. Draxinger, W. Wieser, T. Klein, M. Petermann, and R. Huber, "Analysis of FDML lasers with meter range coherence," in *SPIE BiOS*, (SPIE, 100531T.
52. W. Buehl, D. Stojanac, S. Sacu, W. Drexler, and O. Findl, "Comparison of Three Methods of Measuring Corneal Thickness and Anterior Chamber Depth," American Journal of Ophthalmology **141**, 7-12.e11 (2006).
53. C. Zhou, "Apparatus and Method for Space-Division Multiplexing Optical Coherence Tomography," US 9,400,169 B2, WO 2014/088650 A1 (2014).

1. Introduction

Optical coherence tomography (OCT) [1] is a rapidly developing biomedical imaging modality [2-5]. In the past 26 years, increasing imaging speed has been one of the most important development goals in the OCT field. Development of Fourier-domain OCT, including spectral domain OCT (SD-OCT) and swept source OCT (SS-OCT), resulted in a drastic improvement in both imaging speed and sensitivity [6, 7]. Development of new wavelength-tunable laser further pushed the speed limit to multiple millions axial scans per

second (A-scans/s) [8, 9]. High imaging speed benefits various OCT applications, including *in vivo* ophthalmic [9-16], endoscopic [17] and intravascular [18] imaging in which OCT image quality is improved with minimized motion artifacts. With ultrahigh imaging speed, the need for complex numerical correction of motion artifacts is eliminated [19-21]. High imaging speed is also desirable for functional OCT imaging like angiography [22, 23], where repeated scanning or over-sampling are often required. Wide-field imaging has been widely adopted in OCT applications including ophthalmic imaging [9, 10, 13-16, 24], angiography [25, 26] and bulk tissue imaging [27, 28] in which a large imaging area is often needed to cover the targeted sample with a size of 1 cm^2 or more. With wide imaging field, the need for multiple image acquisition and mosaicking of small-size OCT data obtained at different locations is minimized [29-31].

Current high-speed OCT systems rely mainly on the use of wavelength-tunable lasers such as short cavity lasers with polygon-grating filters [32] or Fabry-Perot tunable filters [33, 34], Fourier-domain mode-locked laser (FDML) [8], vertical-cavity surface-emitting laser (VCSEL) [9], and akinetic programmable swept source [28, 35]. However, the use of faster wavelength-tunable lasers brings in new challenges to maintain the performance of these high-speed OCT systems, considering a drop-off in system sensitivity due to reduced number of photons from each sample location within the dwell time, and limited axial resolution due to the challenge to maintain broad wavelength ranges for ultrahigh laser sweep [2, 5].

Instead of solely pushing the speed limit of wavelength-tunable lasers, a feasible alternative approach is parallel imaging, which utilizes multiple beams to image different segments of the sample simultaneously in order to achieve high imaging speed. A conventional approach to realize parallel imaging is to simply utilize multiple sources and/or multiple sample arm to illuminate different parts of the sample [8, 36-39]. Unfavorable cost scaling with multiple system setups, increased complexity and difficulty for system alignment are the main limitations of conventional parallel imaging techniques. Interleaved OCT (iOCT) based on spectral encoding is a parallel imaging technique which utilizes a single wavelength-tunable source and detector to achieve multi-fold speed improvement [40-43]. However, short separation between the beams in iOCT could lead to cross-talk between the channels. There was also a trade-off observed between sensitivity and imaging speed due to reflectivity of virtually imaged phased array (VIPA).

Recently, we have developed a parallel OCT imaging method, namely space-division multiplexing OCT (SDM-OCT) [44], also based on a single source and detection unit. In SDM-OCT, the sample arm beam was split into multiple channels, with different optical delays in each channel in order to generate multiplexed interference signals that can be detected simultaneously. Split beams were used to image different segments of the sample hence the imaging speed was increased by a factor equal to the number of beams. A high imaging speed of 800,000 A-scans/s was demonstrated in the first prototype system by creating eight-beam illumination using a long-coherence-length VCSEL laser running at 100 kHz.

Although SDM-OCT offered scalable speed improvement with a simple system configuration, the first lab prototype SDM-OCT required extensive time and manual efforts to assemble custom fiber components and control optical delays for each channel, which limits the broad dissemination of the SDM-OCT technology. To construct SDM-OCT easy and reliably, we seek to assemble these components in an integrated photonic chip. Integration of components onto a photonic chip has advantages of cost, size and stability of the system [45]. The progress in nano/micro-fabrication of these photonic integrated circuits (PICs) has leveraged on the significant advancement in the Si-based processing capabilities, which in turn results in significant cost reduction in large scale manufacturability of such technology. The PICs also provide the ability to achieve new functionalities with increased yield and reduced errors in packaging. Integration of OCT components such as interferometer [45-47] and spectrometer [48] onto a photonic chip has been previously reported. In the case

of SDM-OCT system, using a PIC chip to replace fiber-based space-division multiplexing components is potentially advantageous, since custom optical delays and spacing between each output beam can be precisely defined lithographically with sub-micron tolerances during the fabrication process.

In this study, we demonstrated a new prototype of high-speed SDM-OCT system with an integrated photonic chip. The chip measures close to the size of a US quarter coin. A three-layer cascade of 1×2 splitters were integrated in the chip to split the single incident beam into 8 beams. An optical delay of ~2.5 mm on the chip was added between each waveguide channel in order to generate multiplexed interference signals. An eight times increase in imaging speed, reaching ~800,000 A-scans/s, was achieved with the chip-based SDM-OCT system as compared to a single-spot SS-OCT with the same VCSEL running at 100 kHz. A sensitivity of ~91 dB was measured with the chip-based SDM-OCT. The feasibility of high-speed chip-based SDM-OCT was demonstrated with wide-field imaging capabilities. Three-dimensional (3D) volumetric images (700 × 1200 A-scans) of *ex vivo* porcine eye and *in vivo* human finger print covering a large imaging area of up to 18.0 × 14.3 mm^2 was obtained in ~1 second. High-definition 3D OCT images (1500 × 1600 A-scans) of human finger nail were acquired in ~3 seconds. Integrated photonic devices can be reliably manufactured with high precisions and low per-unit cost, facilitating the deployment and adoption of the SDM-OCT technology.

2. Methods

2.1 Prototype SDM-OCT with an integrated photonic chip

Figure 1A shows a schematic diagram of the chip-based SDM-OCT system. In this prototype, fiber-based components, including a planar light wave circuit splitter and a fiber array with different optical delays, were replaced by an integrated photonic chip. The layout of the silicon-based photonic chip is shown in Fig. 1B. The incident beam was coupled into the chip with an optical fiber. A three-layer cascade of 1×2 splitters were used to split the incident light from 1 to 8 beams (Fig 1B), with red dashed lines indicating each layer of splitters. Each beam was then transmitted in a separate waveguide channel. Optical delays were added by setting different lengths for each waveguide channel, with a physical length difference of ~2.5 mm in the waveguide or ~3.7 mm optical delay in air between adjacent channels. The output spacing was set to 250 μm to minimize cross-talk between channels (Fig 1C). The output of the waveguide chip was 8° angle polished to reduce back reflections. The overall size of the integrated photonic chip was ~2.5×2.0 cm^2, close to the size of a US quarter coin (Fig 1D).

The rest of the chip-based SDM-OCT system is described as follows. A booster optical amplifier (BOA, BOA1130s, Thorlabs Inc., USA) was employed right after the commercial VCSEL wavelength-tunable laser (SL1310V1, Thorlabs Inc., USA) to boost the laser output from ~27 mW to ~100 mW. The amplified light was passed through a 95/5 optical coupler, with 5% of the light delivered to a custom Mach-Zender interferometer (MZI) with a ~38.7 mm optical delay in air for phase calibration and 95% of the light used for OCT imaging. The light for OCT imaging was further divided by a 90/10 optical coupler, with 10% of the power sent to the reference arm and 90% of the power used in the sample arm. The incident sample arm beam was coupled into the integrated photonic chip directed through a circulator (AC Photonics, Inc.) and a polarization controller. The 8-beam output of the chip was collimated. A telescope setup with a 30 mm lens and a 50 mm lens was used to expand the beam size. A large scan lens (LSM05, Thorlabs Inc., USA) was mounted in the sample arm after the XY galvanometer mirrors to achieve wide-field volumetric imaging with SDM-OCT. The scan lens had an effective focal length of 110 mm

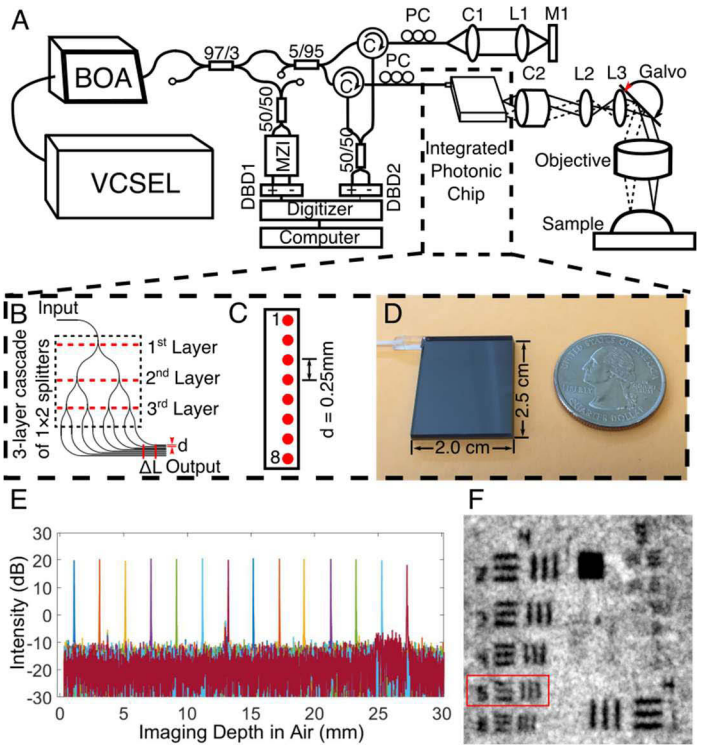

Figure 1. (A) Schematic arrangement of SDM-OCT setup with an integrated photonic chip. (B) Layout of the photonic chip. Input and output of the chip was labeled. A three-layer cascade of 1×2 splitters were shown. Red dashed lines indicate 3 layers of 1x2 splitters, respectively. After 3 layers of splitters, the incident light was split from 1 to 8 beams. Optical delay (ΔL) was ~2.5 mm on the chip. (C) Zoom-in view of output port of the chip showing eight waveguide channels with a d = 0.25 mm spacing between them. Output channels were 8° angle polished to reduce back reflections. (D) Photograph of the chip. The chip measures 2.5 × 2.0 cm^2, close to the size of a US quarter coin. (E) Roll-off measurement of the central beam of the chip-based SDM-OCT in logarithmic scale. Imaging depth range of the system was measured to be ~31.6 mm in air. A roll-off of ~2dB was observed over ~27 mm depth range in air. (F) Transverse resolution was measured to be ~20 μm with a USAF target (Group 4, element 5 is clearly visible). C: Circulator; C1, C2: collimator; DBD1, DBD2: dual balanced detectors; L1, L2, L3: lenses; M1: mirror; PC: polarization controller.

and a working distance of 93.8 mm, resulting in a ~1.7 mm spacing between the adjacent beams at the focal plane and a transverse resolution of ~20 μm as measured with a USAF target (Fig 1F, group 4, element 5). Incident power on the sample was ~3 mW for each beam. Reflected signals from both sample arm and reference arm were routed to a 50/50 optical coupler via optical circulators. Interference signals from both OCT and MZI were detected by dual balanced detectors (PDB480C-AC, 1.6 GHz, Thorlabs Inc.) and their outputs were acquired simultaneously by a dual-channel high-speed data acquisition card (ATS 9373, Alazar Technologies Inc.) operating at a sampling rate of 1.5 GS/s. The sampling rate was estimated by calculating the fringe frequency based on information such as the sweep rate and tuning range of the laser, and total imaging depth needed by 8 parallel imaging channels. The sampling rate was kept at least twice of the maximum fringe frequency to fulfill the Nyquist sampling requirement. Total imaging depth measured was ~31.6 mm in air or ~23.8 mm in tissue, which was sufficient to cover the OCT signals from all the 8 beams separated with different optical delays.

The result of a sensitivity roll-off measurement for the central beam was shown in Fig 1E. The sensitivity of the chip-based SDM-OCT was measured as ~91 dB with a calibrated

-47.2 dB reflector as the sample. A roll-off of ~2 dB was observed over ~27 mm depth range. The axial resolution was maintained as ~11 μm in air or ~8.3 μm in tissue throughout the entire imaging depth. The performance of the current prototype was similar with the one of our first lab prototype [44].

2.2 Scanning protocols for wide-field SDM-OCT volumetric imaging

We employed two scanning protocols for wide-field OCT volumetric imaging: (1) Fast-scanning mode: OCT volumetric data, consisting a total number of 700 × 1200 A-scans for all eight beams (700 x 150 A-scans was acquired for each beam), was obtained in ~1 second. This helps minimize motion artifacts, especially for *in vivo* imaging. (2) High-definition mode: OCT volumetric data, which consisted of 1500 × 1600 A-scans for all eight beams (1500 x 200 A-scans was acquired for each beam) was obtained in 3 seconds in order to achieve Nyquest sampled transverse resolution and preserve details of the sample. The size of each OCT volumetric data was ~3.3 GB in fast-scanning mode and ~9.3 GB in high-definition mode. During the scanning, each beam was moved up to ~18 mm in the fast scanning axis direction, and ~2.4 mm in the slow axis direction. Wide-field OCT data was obtained by stitching 3D OCT images from all 8 beams.

2.3 Image processing for SDM-OCT data

We processed the data following a standard protocol for swept-source OCT [24, 44, 49]. During the phase calibration step, we utilized simultaneously-acquired MZI signal to resample OCT signal linearly in wavenumber space, following a well-established procedure described in [24]. Cross-sectional OCT frames were generated, with sample images from 8 beams showing at separate depth ranges (Fig 2A, 3B, 4B). We then performed a manual 3D stitching of OCT images from 8 beams. Images from 8 beams were cropped out from the cross-sectional frames and aligned along the slow axis direction. Percentage of overlap between images were determined by registering visible features of the sample in overlapping regions. In the overlapping region between two sample beams, we use 50% of data from each sample image to form the final stitched image. After alignment and stitching, a global intensity correction was applied to the 3D data to correct for stripe-like intensity distributions that were caused by intensity variation between different beams. Each strip of stitched data was first thresholded to remove speckle noise. Next, pixels above the threshold in each strip were averaged to get a mean value. Then, pixel intensities in each strip were normalized to its mean value. A local intensity correction was applied to *en face* averaged images (Fig 2D, 3F, 4E) to correct for the intensity variation due to defocusing of beams on the sample with large surface curvature. The *en face* image was first divided into small grids. Next the mean value of each grid was calculated. Then, each grid was normalized to its mean value. All the above mentioned processing steps were automatically performed with a custom Matlab code.

3. Results

3.1 Fast-scanning ex vivo imaging of the anterior segment of a porcine eyeball

High-speed imaging using chip-based SDM-OCT was first demonstrated by imaging *ex vivo* on the anterior segment of a porcine eyeball. A fresh piglet (~ 8 weeks old) eyeball was obtained from a local abattoir and preserved in Dubecco's Modified Eagle's Medium (DMEM, Gibco). SDM-OCT imaging was performed within a few hours of sacrifice. To image the entire eyeball, each beam was scanned ~13.5 mm and ~2.4 mm in the fast and slow axis directions, respectively. The total imaging area covered by eight beams was ~13.5×14.3 mm^2, considering a ~29% overlap between scanning areas by adjacent beams. Fast-scanning

protocol was employed to image the eyeball. The results of anterior segment imaging were shown in Fig. 2. Fig. 2A showed a single cross-sectional (B-scan) SDM-OCT image of the anterior segment of the piglet eyeball, with images from eight beams acquired simultaneously. Acquired depth-resolved SDM-OCT images of the piglet eyeball appeared simultaneously at eight depth ranges, as indicated by the rainbow color bands at the left side of the Fig. 2A. The red band indicated the acquired image from the 1st beam located close to zero-delay/zero imaging depth in the SDM-OCT image. The magenta band showed another acquired OCT image from the 8th (last) beam, which was located at the imaging depth of ~20 – 22 mm of the SDM-OCT image. The set optical delay between adjacent beams in this photonic chip were sufficient to cover the whole anterior chamber of the piglet eyeball with no overlapping between neighboring images in the axial direction. Notice that the eyeball images from edge beams (1st and 8th) were not as clear as those images from central beams. This was attributed to the defocusing of the edge beams where the focal planes were out of the sample surface due to the steep surface curvature of the eyeball. Since most of cornea regions of the piglet eyeball were covered by central beams while edge beams covered mainly sclera regions, influence of the defocusing effect of the edge beams was minimized. Next, piglet eye images from all 8 beams were stitched together to generate a 3D volume rendering of the anterior segment. Cross-sectional (B-scan) views of the final stitched anterior segment image along the slow and fast-scanning axes were shown in Fig. 2B and 2C, respectively. The color bands on the bottom of Fig. 2B

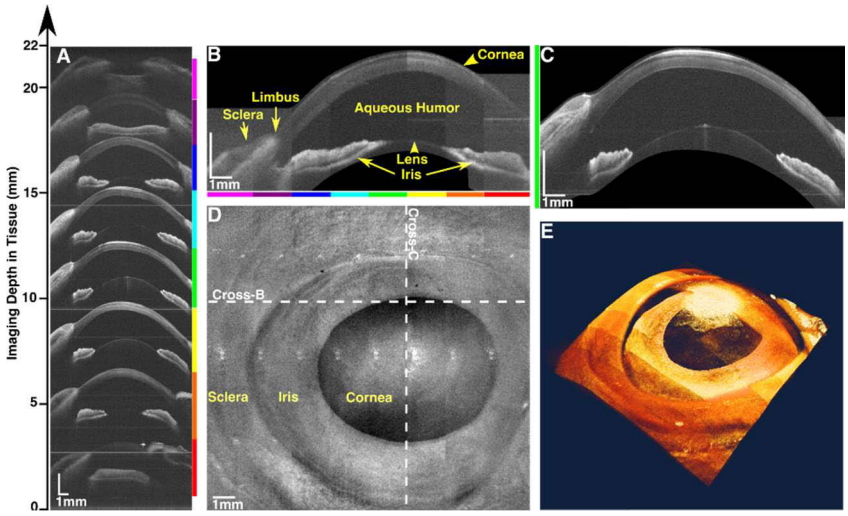

Figure 2. Chip based SDM-OCT image of *ex vivo* porcine eyeball of area ~13.5×14.3 mm^2 with fast scanning protocol consists of 700×1200 A-scans/s. (A) A single 2D cross sectional B-scan (average of 10 frames) showing 8 images corresponding to 8 beams appear at different depths. Eight images cover a depth range of ~22 mm in tissue (black regions on top and bottom of the image were cropped). Different color bands at the left of the B-scan represent imaging area covered by each beam, red color shows imaging area covered by the first beam and violet color represents the imaging area covered by the last beam. (B) 2D cross-section of final image of 8 stitched beams, color bands on the bottom show area of the image acquired by each beam. (C) Cross sectional image of the single beam cropped out of a single B-scan. (D) *En face* image of the final stitched image, horizontal and vertical dashed lines show the directions of 2D cross sectional images shown in (B) and (C) respectively. (E) 3D volumetric reconstruction of anterior chamber of the eyeball using final stitched image (Visualization 1).

denoted the origin of each section of the stitched image from the SDM-OCT image (Fig. 2A). The green band on the left of the Fig. 2C indicated that it was the zoomed-in image of the same section in Fig. 2A. Since the aqueous humor in the anterior chamber was transparent, incident beams could transmit through the piglet cornea and arrived at the iris and the lens.

Cornea, iris, top surface of the lens, sclera and limbus surrounding the anterior chamber of the piglet eye were clearly visualized in these two cross-sectional images. The *en face* averaged image of the final stitched data clearly showing cornea, iris and sclera parts of the eyeball was presented in Fig. 2D. Two dashed lines in the vertical and horizontal directions illustrated the directions of the cross-sectional images shown in Fig. 2B and 2C. Furthermore, a 3D volumetric rendering of the anterior segment of the piglet eye was reconstructed using the entire data set (Fig. 2E), with a video demonstrating the 3D reconstruction in Visualization 1 of the supplementary material.

3.2 Fast-scanning in vivo wide-field imaging of human fingerprints

Wide-field imaging of the high-speed chip-based SDM-OCT system was also demonstrated *in vivo* to scan human fingerprints in 3D. The middle finger of a healthy volunteer was facing up and held steady on the sample stage using a black foam. Eight beams were illuminated on different spots of the finger, as shown in Fig. 3A. Each beam

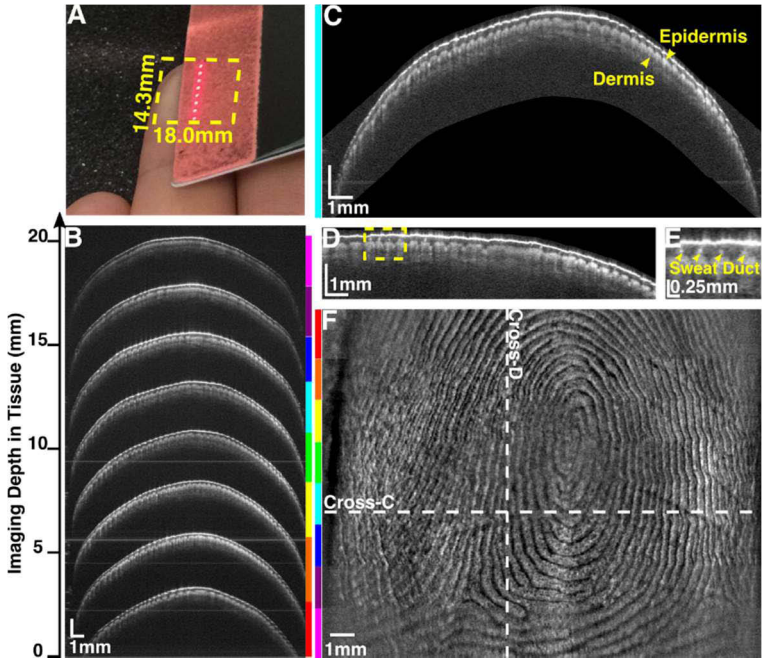

Figure 3. Chip based SDM-OCT *in vivo* wide-field human fingerprint imaging of area 18.0×14.3 mm^2 with fast scanning protocol consists of 700×1200 A-sans/s. (A) Photograph of middle finger print showing 8 beams illumination, rectangular box defines imaging area. (B) A single 2-D cross sectional B-scan (average of 10 frames) showing 8 images corresponding to 8 beams appear at different depths. Different color bands at the left of the B-scan represent imaging area covered by each beam, red color shows imaging area covered by the first beam and violet color represents the imaging area covered by the last beam. (C) 2D cross sectional image of the single beam. (D) 2D cross-section of final image of 8 stitched beams. (E) Enlarged area of the cross section of final stitched image showing sweat ducts. (F) *En face* view of the final stitched image, horizontal and vertical dashed lines show the directions of 2D cross sectional images shown in (C) and (D) respectively. Color bands on the left side of the image denote area of the image acquired by each beam. 3D rendering of the fingerprint image can be found in Visualization 2.

was scanned ~18 mm in the fast axis direction to cover the finger width and ~2.4 mm in the slow axis direction. The total imaging area covered by all 8 beams was ~18×14.3 mm^2 after compensating ~29% overlap along the slow axis. Fast scanning protocol was employed for this demonstration and the whole 3D data set was acquired in ~1 second. Fig. 3B shows a

single cross-sectional (B-scan) SDM-OCT image demonstrating eight different segments of the finger from the eight beams. Images from all the 8 beams were of similar quality because of the relatively flat surface of the finger along the slow axis direction. A zoom-in image from the cyan band of SDM-OCT image was shown in Fig. 3C. Epidermis and dermis layers of the skin were clearly differentiated. Connected friction ridges across the finger were also clearly visible. The cross-sectional view of the final stitched image of the finger along the slow axis was shown in Fig. 3D, with a zoom-in view of the yellow rectangle region in Fig. 3E clearly showing fine features such as sweat ducts. Fig. 3F depicted an *en face* projection of the finger, with color bands on the left indicating regions of the image scanned by each beam. A whorl pattern of the fingerprint was clearly recorded by SDM-OCT. Dashed horizontal and vertical lines in the *en face* image referred to the locations of obtained cross-sectional images in Fig. 3C and D, respectively. A video showing 3D volumetric reconstruction of the fingerprint was provided in Visualization 2.

3.3 High-definition in vivo wide-field imaging of human finger nail

We also demonstrated wide-field, *in vivo* imaging of human finger nail in high-definition scanning mode. High-definition scanning protocol was employed to scan the nail fold of a volunteer's middle finger. Each frame had 1500 A-scans and each volume had 1600 frames (i.e. each beam contributed 200 frames), resulting in a total image acquisition time of ~3 seconds. The total scanning area was ~18×14.3 mm^2. Hence, transverse pixel sizes for both fast and slow axis directions were ~12 μm. Results were shown in the Fig. 4. A photograph showing 8 beams illumination on the nail side of the middle finger was shown in Fig 4A. Among eight different segments of the cross-sectional SDM-OCT image of the finger nail shown in Fig 4B, five of them were obtained from the finger nail regions and three of them were obtained from the neighboring skins. The indication of color bands in Fig. 4 was the same as those illustrated in Fig. 2 and Fig. 3. A zoom-in view of the cyan band of SDM-OCT was shown in Fig 4C, showing the beginning of the finger nail region. Finger nails located at the center of Fig 4C, with layers of the nail plate, the nail bed and the nail matrix discernible with clearly edges. On the sides of the nail region, connected finger skin was observed with separated epidermis and dermis layers. Fine features such as the proximal nail fold and the cuticle were also visible. Fig. 4D showed the other cross-sectional view of the final stitched image along the slow axis, showing the clear structure of finger nail junction, with the proximal nail fold and the cuticle located in the middle of the junction, connecting the skin and the nail. Another fine feature, the vessels in the dermis layer of the skin, was detected in the image as dark curve lines. The *en face* projection of final stitched image was shown in Fig 4E. Curve stripes of the cuticle and the proximal nail fold were discernible below the nail plate. The surface pattern of the skin layer surrounding the nail was also visible. 3D volumetric rendering of the high-definition human nail data was presented in Visualization 3 in supplementary materials.

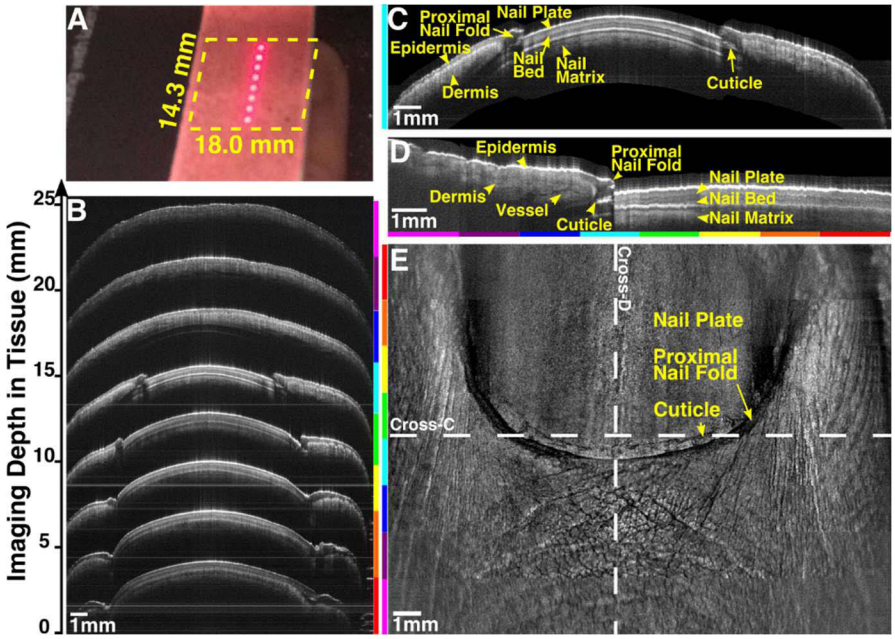

Figure 4. Chip based SDM-OCT *in vivo* wide-field human finger nail imaging of area 18.0×14.3 mm^2 with high definition scanning protocol consists of 1500×1600 A-sans/s. (A) Photograph of nail side of middle finger showing 8 beams illumination, rectangular box defines imaging area. (B) A single 2D cross sectional B-scan (average of 10 frames) showing 8 images corresponding to 8 beams appear at different depths. Different color bands at the left of the B-scan represent imaging area covered by each beam, red color shows imaging area covered by the first beam and violet color represents the imaging area covered by the last beam. (C) 2D cross sectional image of the single beam. (D) 2D cross-section of final image of 8 stitched beams. (E) *En face* view of the final stitched image, horizontal and vertical dashed lines show the directions of 2D cross sectional images shown in (C) and (D) respectively. Color bands on the left side of the image denote area of the image acquired by each beam. 3D rendering of the finger nail image can be found in Visualization 3.

4. Discussion

In this study, we demonstrated a prototype SDM-OCT system with an integrated photonic device. Compared with our first lab prototype SDM-OCT system, the chip-based SDM-OCT has advantages of smaller-size, cost-effectiveness, ease of manufacture and precise control of optical delays over fiber-based SDM-OCT. An 800,000 A-scans/s OCT imaging speed was demonstrated using the chip-based SDM-OCT system. In fact, imaging speed of SDM-OCT can be further improved if the number of parallel imaging beams are increased. State-of-the-art tunable lasers with a long coherence length, *e.g.* akinetic programmable swept sources [28], meter-range VCSEL [50] and tunable-range FDML [51], enable mass imaging parallelization using SDM-OCT. Enhanced imaging speed of SDM-OCT is highly desirable for *in vivo* applications, reducing total imaging time, minimizing motion artifacts while achieving a wide imaging field of view.

Imaging depth range for each beam in the SDM-OCT system depends on the optical delay between adjacent imaging channels. The current chip-based system has an optical delay of ~3.7 mm in air (~2.8 mm in tissue). In most scattering tissue, light penetration is ~1 - 2 mm below the tissue surface. Optical delays of the current chip-based system is sufficient for most of these applications. In our current images of porcine eye balls and human fingers, no overlapping regions were observed. However, we do notice that in some regions images from adjacent beams are close to each other (Fig. 2A, the 2nd and the 3rd images from the top), which makes it difficult to separate individual images. It is possible that two adjacent regions

in the SDM-OCT image may overlap if imaging range needed on sample is long or the sample surface is complex, e.g. surface with both positive and negative curvatures, or surface with a steep curvature. For example, in the case of human anterior segment imaging, the current system with a ~2.8 mm optical delay in tissue may not be sufficient, considering the average human anterior chamber depth of ~ 3.3 mm and the average human corneal thickness of ~0.53 mm [24, 52]. In the future, new photonic chips with a longer optical delay may be custom developed according to the requirement for specific applications in order to avoid possible overlaps.

The sensitivity of the chip-based SDM-OCT system is affected by several factors, including the exposure time, the optical power illuminating on the sample, quantum efficiency of the detector, and transmission loss in the photonic chip and optical components. The theoretical shot-noise-limit sensitivity is calculated by [2, 5]

$$S = 10\log\left(\frac{\rho PT}{e}\right) - \mathrm{IL}, \quad (1)$$

where ρ denotes the quantum efficiency of the detector, P denotes sample arm power, T denotes the dwell time at each sample location, e is the elementary charge of an electron, and IL denotes backward transmission loss from the sample to the detector. SDM-OCT preserves the dwell time at each imaging spot while increases OCT imaging speed through parallel imaging with multiple sample beams. For example, the dwell time of an 8 channel SDM-OCT system using a 100 kHz swept source laser is 10 us, which is 8 times longer compared to a single beam OCT system operating at 800 kHz (dwell time at each imaging spot is 1.25 us). Eight times more back-scattered photons may be collected from each imaging spot using SDM-OCT compared to a single beam OCT system running at the same A-scan rate. This may lead to a significant sensitivity advantage for SDM-OCT. However, the sensitivity of the current prototype SDM-OCT system was greatly affected by backward transmission loss in the sample arm, especially the insertion loss at the input and output ports of the photonic chip, and the splitting loss within the chip. In the forward direction, input power to the chip was ~ 70 mW and the sample arm power for each beam was ~ 3 mW (total ~24 mW for 8 beams). This translated to ~4.5 dB light loss, including insertion loss of the chip and transmission loss of optical components. In the backward direction, a similar amount of transmission / insertion loss from was expected. Additionally, the three-layer cascade of 1×2 splitters inside the photonic chip (Fig 1B) would introduce a 3 dB splitting loss at each layer, resulting in a ~9 dB loss in the backward transmission. The ~91 dB sensitivity measured from the current chip-based SDM-OCT system was ~15 dB lower than the calculated shot-noise-limited sensitivity. The above mentioned transmission and splitting loss attributed to ~13.5 dB (*i.e.* 4.5 dB + 9 dB) sensitivity loss. The rest of backward loss was attributed to the return insertion loss at the output port of the chip, where the back-scattered light was coupled into the chip from free space. A low-loss design using circulators or couplers to bypass cascaded splitters in the return path may be used to significantly improve the sensitivity of SDM-OCT [53]. This is currently under development.

Optical clock (OC, k-clock) is widely used for SS-OCT since linear sampling of fringe in wavenumber provided by OC eliminates the need for additional data acquisition of MZI signals and additional post-processing step for phase calibration [36, 49]. However, the current optical clock provided by the swept source laser has limited frequency range (~500 MHz) and the supported OCT imaging depth range (~12 mm) is not sufficient for our applications, which require more than 30 mm imaging depth range in air. In the current study, both the MZI and OCT signals were still acquired at the same time. A custom high-frequency MZI-OC setup is being developed for future applications.

5. Conclusions

In summary, we demonstrated a new prototype high-speed SDM-OCT system using an integrated photonic chip. An eight times increase in imaging speed was achieved with the chip-based SDM-OCT system employing an eight-beam parallel illumination. A sensitivity of ~91 dB was measured with the chip-based SDM-OCT system. We demonstrated the prototype chip-based SDM-OCT for wide-field (up to 18.0 x 14.3 mm^2) imaging applications. Fast scanning 3D OCT images of *ex vivo* porcine eyeball and *in vivo* human fingerprint (700 × 1200 A-scans) were acquired in ~1 second. We also demonstrated a high-definition 3D OCT scan of a human finger nail (1500 × 1600 A-scans) in 3 seconds. Incorporating integrated photonic devices in SDM-OCT has the advantages in lowering the per-unit cost and facilitating the broad dissemination of the SDM-OCT technology. The continuing progress in advanced nanofabrication of Silicon PICs – leveraging on communications and computing applications - will accelerate the wide adoption of this PIC-based approach in SDM OCT. The integration of III-V on Silicon PICs has also been pursued for systems-on-chip in computing and communications, and such advanced integrated technologies can be leveraged in future integration.

Funding
This work was supported by NSF DBI-1455613 (IDBR Award to C.Z.), IIP-1623823 (I-Corps grant to C.Z.), IIP-1640707 (PFI:AIR-TT Award to C.Z.), ECCS-1408051 (N.T.), NIH K99/R00 EB-010071 (C.Z.) and R21 EY-026380 (C.Z.) grants, and Lehigh University Start-up fund and CORE grant and D. E. ’39 and P. M. Smith Endowed Chair Professorship Fund (N.T.).

Acknowledgements

The authors thank Lian Duan, Zhao Dong, Jason Jerwick, and Penghe Wu for helpful discussion.

Disclosures
CZ: SDM Innovations, Inc. (I, P, S); AN, AW: Tornado Spectral Systems, Inc. (E); Other authors declare that there are no conflicts of interest related to this article.